

RSC Advances



This is an *Accepted Manuscript*, which has been through the Royal Society of Chemistry peer review process and has been accepted for publication.

Accepted Manuscripts are published online shortly after acceptance, before technical editing, formatting and proof reading. Using this free service, authors can make their results available to the community, in citable form, before we publish the edited article. This *Accepted Manuscript* will be replaced by the edited, formatted and paginated article as soon as this is available.

You can find more information about *Accepted Manuscripts* in the [Information for Authors](#).

Please note that technical editing may introduce minor changes to the text and/or graphics, which may alter content. The journal's standard [Terms & Conditions](#) and the [Ethical guidelines](#) still apply. In no event shall the Royal Society of Chemistry be held responsible for any errors or omissions in this *Accepted Manuscript* or any consequences arising from the use of any information it contains.

Reduced Graphene Oxide Coupled CdS/CoFe₂O₄ Ternary Nanohybrid for Enhanced Photocatalytic Activity and Stability: A Potential Role of Reduced Graphene Oxide as a Visible Light Responsive Photosensitizer

Simrjit Singh and Neeraj Khare*

Department of Physics, Indian Institute of Technology Delhi, Hauz Khas, New Delhi, 110016, India.

Abstract

We report the coupling of CdS/CoFe₂O₄ (CdS/CFO) core/shell nanorods heterostructure on the 2D platform of reduced graphene oxide (RGO) sheets by a facile soft chemical route. Intimate interfacial contacts between CdS, CFO and RGO are achieved in the synthesis. The CdS/CFO/RGO nanohybrid exhibits enhanced photocatalytic activity for the degradation of methylene blue under visible light irradiation. In addition to enhanced photocatalytic activity, this trio-coupled nanocomposite exhibit enhanced photostability and is magnetically separable from the aqueous solution due to the presence of the CFO in the composite nanostructure and thus can be used for repeated operations of the photocatalytic process. A mechanism for the enhanced photocatalytic activity of CdS/CFO/RGO has been proposed where the RGO in the ternary nanocomposite serves as a visible light responsive photosensitizer. Our present work indicates that the careful choice of the semiconductor coreshell nanostructures and its coupling with reduced graphene oxide have a greater potential in the designing of efficient and stable visible light responsive photocatalytic materials.

KEYWORDS: CdS, CoFe₂O₄, Graphene, Coreshell nanostructures, Photosensitizer.

a) Author to whom all correspondence should be addressed.

Electronic mail: nkhare@physics.iitd.ernet.in

1. Introduction

The worldwide shortage of energy and hazardous environmental pollutants have attracted a lot of interests of the scientific community for the research on semiconductor photocatalysis as a green energy technology for the generation of hydrogen and degradation of organic pollutants using the abundant solar energy.¹⁻³ Among the various semiconductor materials, TiO₂ and ZnO have been widely used and considered as suitable photocatalytic materials due to their high stability, low cost and strong oxidizing power.^{4,5} However, the major drawback in using these semiconductor materials is their large bandgaps ($E_g \sim 3.2$ eV) due to which they utilize only UV light (~4-5 % of the solar spectrum) and significantly limits the use of visible light portion (~46 %) of the solar spectrum.^{6,7} Therefore, the current research interest focuses in the designing of visible light active photocatalyst materials with enhanced photocatalytic activity and photostability.

Formation of heterojunction between two semiconductor materials of different band gaps is a novel strategy to improve the separation efficiency of the photogenerated charge carriers.⁸⁻¹¹ The coupling of semiconductor materials with a type-II band-edge alignment, where the conduction band of one of the semiconductors lies in between the conduction and valence bands of the other semiconductor, results in easy separation of the photo-generated charge carriers at the interface and leads to enhancement in the photocatalytic activity.¹²⁻¹⁴

Recently, the coupling of graphene with semiconductor materials has also been considered as a promising strategy for improving the photocatalytic activities of the semiconductors. Graphene, due to its excellent charge carrier mobility (~ 200000 cm²V⁻¹s⁻¹), high electrical conductivity ($\sim 10^6$ S cm⁻¹) and high work function (-4.42 eV) accepts photogenerated electrons from the conduction bands (CBs) of most of the semiconductors¹⁵ and act as an electron transporter and thus significantly suppresses the recombination rate of the photogenerated charge carriers in the

semiconductors resulting in enhanced photocatalytic activity.^{16,17} Besides the conventional use of graphene as an electron acceptor and transporter, some recent theoretical and experimental studies on wide band gap semiconductor-graphene nanocomposites show a promising role of graphene as a visible light responsive photosensitizer.¹⁸⁻²⁰ However, in these composite the wide band gap semiconductors are unable to be photoexcited under visible light irradiation and only the photosensitization role of graphene provides charge carriers for the photocatalytic degradation of contaminants. Graphene as a photosensitizer can be coupled with suitable visible light active semiconductor materials which can lead to highly efficient photocatalytic process for the degradation of organic pollutants under visible light irradiation. In comparison to graphene-semiconductor binary systems,^{21,22} recently the graphene based ternary nanocomposites have shown greater potential to enhance significantly the photocatalytic process.²³⁻²⁵

In the present work, we have synthesized a core/shell nanoheterostructure of visible light responsive semiconductor materials i.e. CdS ($E_g \sim 2.4$ eV) as a core material and CoFe_2O_4 ($E_g \sim 1.8$ eV) as a shell material and coupled this core/shell nanoheterostructure with reduced graphene oxide (RGO) by using soft chemical routes. A substantial enhancement in the photocatalytic activity and photostability of the ternary nanohybrid (CdS/CFO/RGO) photocatalyst material is demonstrated under visible light irradiation. A reaction mechanism is shown where the synergetic effect of the semiconductor heterojunction and light absorbing properties of the graphene are used simultaneously to account for the enhancement in the photocatalytic activity. A potential role of RGO as a visible light responsive photosensitizer is proposed where the photoexcited electrons from the RGO are transferred to the conduction band of CFO. The presence of chemically stable CFO as a shell material inhibits the photocorrosion of CdS core by avoiding a direct contact of the core with aqueous solution. Also, due to the magnetic nature of

CFO, this trio coupled photocatalyst material can be easily separable from the aqueous solution by applying an external magnetic field which can be useful for large scale applications of this photocatalyst material.

2. Experimental section

2.1. Synthesis of graphene oxide (GO)

Graphene oxide (GO) was synthesized by the modified Hummer's method. For the synthesis, 1 g of graphite powder and 0.5 g of NaNO_3 were put into 30 mL of cold ($0\text{ }^\circ\text{C}$) concentrated H_2SO_4 under stirring. After 30 minutes, 3 g of KMnO_4 was added to the above mixture and the temperature of the mixture was kept below $20\text{ }^\circ\text{C}$. Afterwards, the temperature of the mixture was raised to $35\text{ }^\circ\text{C}$ and stirred for 2 hours followed by dilution with 45 mL of deionized (DI) water. The mixture was stirred for another 1 hour and after that a 50 mL solution containing 40 mL of DI water and 10 mL of 30 % H_2O_2 was added to the above mixture. At this stage the brown color of the solution was turned to bright yellow. The suspension was centrifuged at 8000 rpm for several times and the resulting product was dried in an oven at $60\text{ }^\circ\text{C}$ for 3 hours to obtain the GO powder.

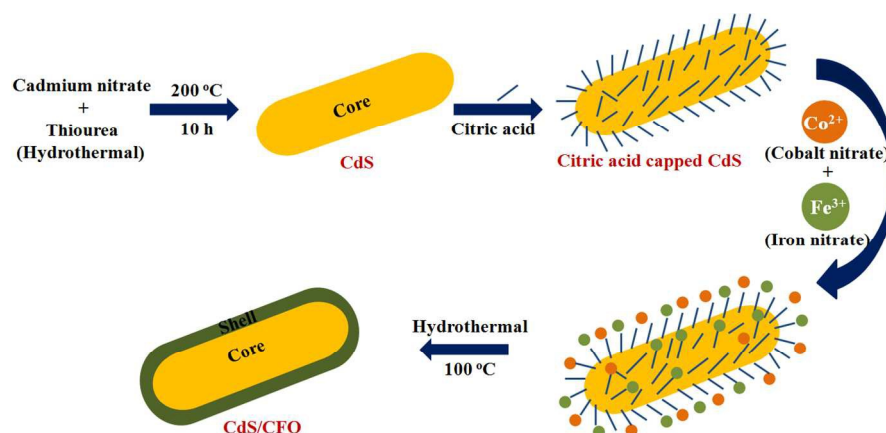
2.2. Synthesis of CdS nanorods

For the synthesis of CdS nanorods, 1.85 g of $\text{Cd}(\text{NO}_3)_2$ and 3.65 g of $\text{CH}_4\text{N}_2\text{S}$ were mixed in 50 mL of ethylenediamine. After 30 minutes of stirring, the mixture was transferred into a 50 mL Teflon lined stainless steel autoclave and was put into an oven for the hydrothermal treatment. The reaction was carried out at $200\text{ }^\circ\text{C}$ for 10 hours. The resulting yellow color paste was washed several times with DI water and dried at $80\text{ }^\circ\text{C}$ to get CdS nanorods.

2.3. Synthesis of CdS/CFO core/shell nanostructure

CdS/CFO core/shell nanorods were synthesized by self assembly using a soft chemical method (Scheme 1a). Firstly, 1 g of CdS nanorods were dispersed into citric acid solution (5 mg mL^{-1}) to functionalize the surface of the nanorods with negatively charged citrate ions. Afterwards, the functionalized CdS nanorods were dispersed into a 30 mL solution of $\text{Co}(\text{NO}_3)_2 \cdot 6\text{H}_2\text{O}$ (0.436 g) and $\text{Fe}(\text{NO}_3)_3 \cdot 9\text{H}_2\text{O}$ (1.212 g) followed by the addition of 5 mL NaOH solution. The mixture was stirred for 3 hours at 100°C . Finally, the resulting solution was subjected to the hydrothermal treatment at 100°C for 3 hours to obtain the CdS/CFO core/shell nanorods.

For comparison, CFO nanostructures were also synthesized by using the above method without CdS nanorods.

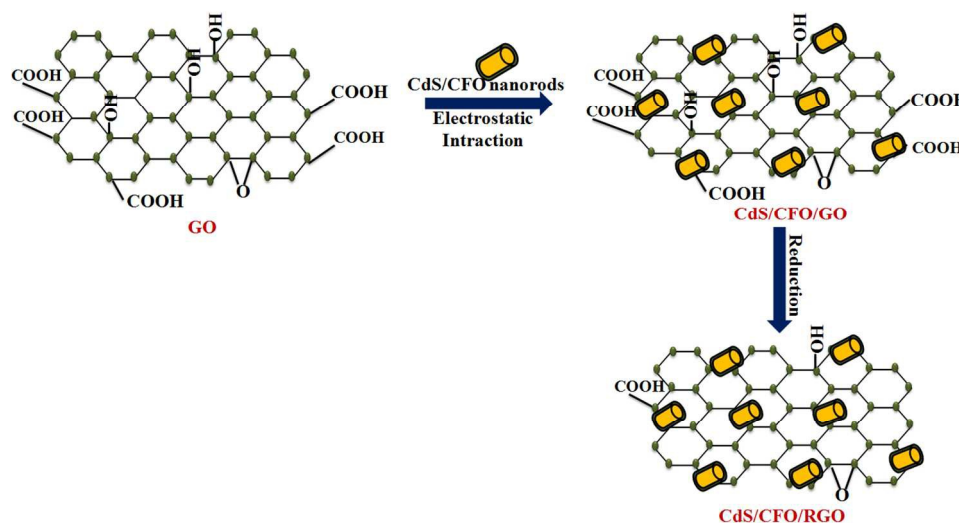


Scheme 1a. Schematic diagram showing different steps in the synthesis of CdS/CFO core/shell nanostructure.

2.4. Synthesis of CdS/CFO/RGO nanostructure

The synthesis of CdS/CFO/RGO is schematically illustrated in Scheme 1b. For the synthesis of CdS/CFO/RGO nanostructure, the CdS/CFO core/shell nanorods suspension (10 mg mL^{-1} in ethylene glycol) was mixed with GO suspension (0.3 mg mL^{-1} in DI water) under magnetic stirring followed by the addition of 4 mL of ammonia solution to maintain the pH of the resulting solution ~ 10 . After half an hour of stirring, 2 mL of the hydrazine was added to the above

solution to reduce the graphene oxide. Finally, the solution was kept at 80 °C in an oil bath for 6 hours. The resulting paste was washed with deionized water and dried at 60 °C in an oven for 2 hours to obtain CdS/CFO/RGO ternary nanohybrid.



Scheme 1b. Schematic diagram for the synthesis of CdS/CFO/RGO nanostructure.

2.5. Characterization methods

X-ray diffractometer (XRD, Rigaku Ultima-IV) with $\text{CuK}\alpha$ ($\lambda = 1.54 \text{ \AA}$) irradiation was used for the structural characterization of the synthesized nanostructures. X-ray photoelectron spectroscopy (XPS, Specs, German company) measurements were done to study the chemical states of the elements. Transmission electron microscopy (TEM, JEOL, JEM-2200-FS) was used to study the morphology of the nanostructures. UV-visible spectrophotometer (Perkin Elmer, LAMBDA-1050) was used to record the optical absorption spectra of the dye solution and the optical bandgap of the nanostructures. Raman spectra of the nanostructures were recorded using Raman Spectrometer (Horiba Jobin Vyon, LabRam HR Evolution with Argon ion laser source). The photoluminescence spectra were recorded using He-Cd laser source. The photo current density and electrochemical impedance spectroscopy (EIS) measurements were done using a photoelectrochemical workstation (Zahner Zennium, PP 211). A conventional three electrode

cell assembly was used for the measurements where Pt wire and Ag/AgCl were used as counter and reference electrodes respectively. Thin films of the samples coated onto Fluorine doped Tin Oxide (FTO) substrates were used as working electrodes. For this, 20 mg of the sample was dissolved in the 20 ml of isopropanol and ultrasonicated for half an hour for making uniform dispersion of the sample. The thin films of the samples were spray coated onto FTO substrate which was placed onto hot plate at 80 °C. A 0.5 M Na₂SO₄ aqueous solution was used as an electrolyte.

2.6. Photocatalytic measurements

Photocatalytic experiments were performed by measuring the photodegradation activities of methylene blue (MB) dye at room temperature under visible light irradiation using a 300W Xenon lamp. A UV cut off filter was used to eliminate the UV light from the light source. For the degradation of MB, 100 mg of catalyst was dispersed in 250 ml of MB dye solution (10 mg L⁻¹). Before illumination, an adsorption-desorption equilibrium between the pollutant and the catalyst was setup by stirring the mixture for half an hour in the dark. After half an hour, the mixture was exposed to visible light irradiation and at regular intervals of time, a 5 ml quantity of the MB solution was withdrawn to examine the change in the concentration of MB. The UV-visible absorption spectrum of the solution was recorded using a LAMBDA-1050 spectrophotometer (Perkin Elmer) to determine the degradation of MB dye in the solution.

3. Results and discussion

3.1. Characterization

Fig. 1a. shows X-ray diffraction (XRD) patterns of CFO, CdS, CdS/CFO and CdS/CFO/RGO nanostructures. The XRD pattern of the CFO nanostructure exhibits diffraction peaks at $2\theta = 30.20^\circ, 35.46^\circ, 37.19^\circ, 43.15^\circ, 53.58^\circ, 57.11^\circ, 62.68^\circ$ which corresponds to the (220), (311), (222),

(400), (422), (511), (440) crystallographic planes of the cubic spinel structure of the CoFe_2O_4 (JCPDS No. 22-1086). The XRD patterns of the CdS, CdS/CFO and CdS/CFO/RGO nanostructures exhibit dominant peaks at 2θ values of 24.7° , 26.5° , 28.1° , 36.6° , 43.8° , 47.9° , 50.9° , 51.8° , 52.9° , 54.5° , 58.4° , 66.8° , 69.4° , 71.0° , 72.5° , 75.7° which can be well indexed to the (100), (002), (101), (102), (110), (103), (200), (112), (201), (004), (202), (203), (210), (211), (114), (212) crystal planes of the hexagonal CdS (JCPDS No. 41-1049). In addition, the peaks observed at 2θ values of 35.6° and 62.9° in CdS/CFO and CdS/CFO/RGO are attributed to (311) and (440) crystal planes of CFO. Notably, no diffraction peak corresponding to RGO phase is observed in the XRD pattern of CdS/CFO/RGO nanostructure, which can be due to the relatively low diffraction intensity of RGO in comparison to the CdS diffraction peaks in the nanocomposite.

Fig 1b shows a shift in the diffraction peak corresponding to (110) plane of CdS in CdS/CFO and CdS/CFO/RGO nanostructures. The shift towards higher Bragg's angles is due to the coating of CFO around CdS and coupling of RGO around CdS/CFO nanostructures which causes shrinkage of CdS lattice.

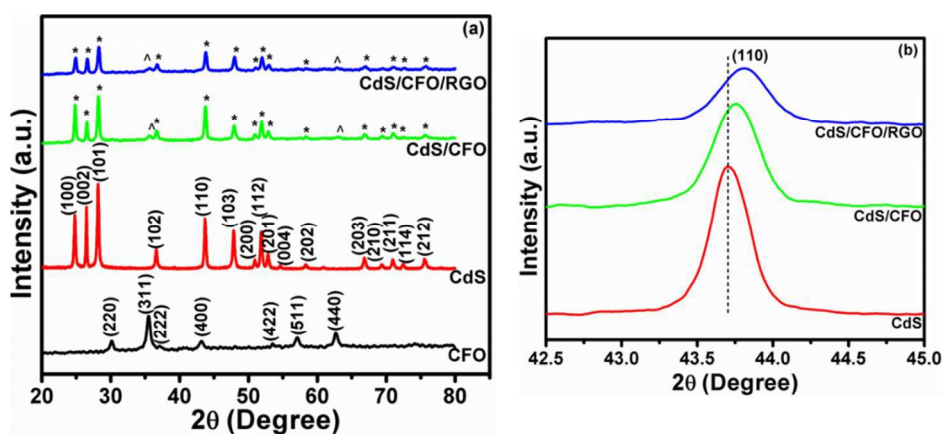


Fig. 1. (a) XRD patterns of the CFO, CdS, CdS/CFO and CdS/CFO/RGO nanostructures. In the core/shell nanostructures, peaks marked with (*) correspond to CdS and peaks marked with (^) corresponds to CFO. (b) Shift in the peak position of the (110) peak of CdS in the CdS/CFO and CdS/CFO/RGO nanostructures.

The reduction of GO to RGO and its coupling with CdS/CFO can be estimated from the Raman study. Fig. 2 shows the Raman spectra of GO, CdS, CdS/CFO and CdS/CFO/RGO nanostructures. The Raman spectra of CdS, CdS/CFO and CdS/CFO/RGO nanostructures exhibit peaks at 300, 601, 905 cm^{-1} corresponding to fundamental optical phonon mode (LO), first overtone mode (2LO) and second overtone mode (3LO) of CdS.²⁶ However, no peak corresponding to CFO has been observed in the CdS/CFO and CdS/CFO/RGO nanostructures which can be due to the presence of very small amount of CFO in the composite nanostructures as confirmed from the XRD results. Raman spectra of GO and CdS/CFO/RGO contain both D- and G-bands which confirm the successful coupling of CdS/CFO with RGO.²⁷ Also, in the CdS/CFO/RGO nanostructure, the increase in the intensity ratio $I_D/I_G = 1.30$ is observed as compared to the intensity ratio (1.04) of GO which suggests the successful reduction of GO in the composite nanostructures.²⁸

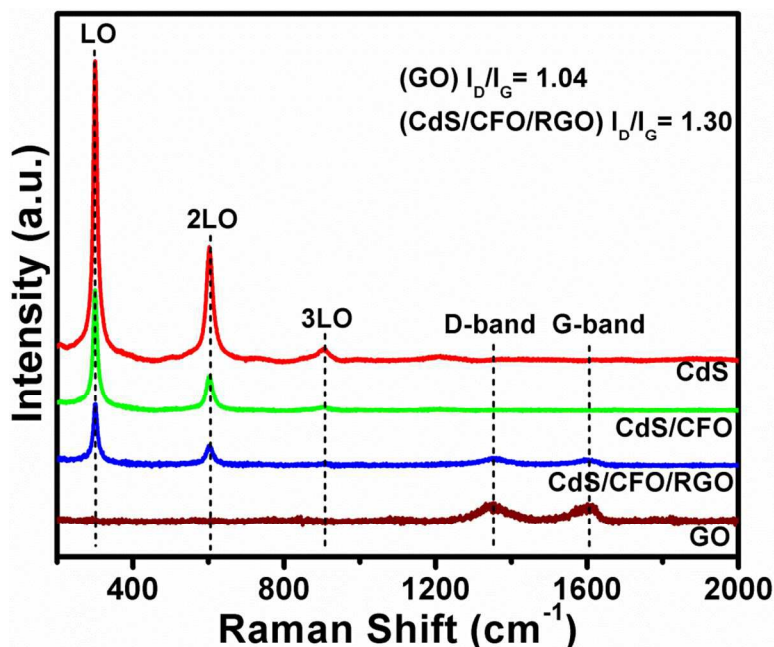


Fig. 2. Raman spectra of CdS, CdS/CFO, CdS/CFO/RGO and GO nanostructures at room temperature.

Fig. 3a-f shows high resolution XPS scans of Cd 3d, S 2p, Co 2p, Fe 2p, O 1s and C 1s in the CdS/CFO/RGO nanostructure respectively. The peak positions centered at 405.2 eV ($3d_{5/2}$), 411.9 eV ($3d_{3/2}$) and 161.9 eV (S 2p) in the XPS scans of Cd (3d) and S (2p) respectively (Fig. 3a and 3b) confirm the presence of Cd^{2+} and S^{2-} chemical states of the respective elements in the form of CdS.

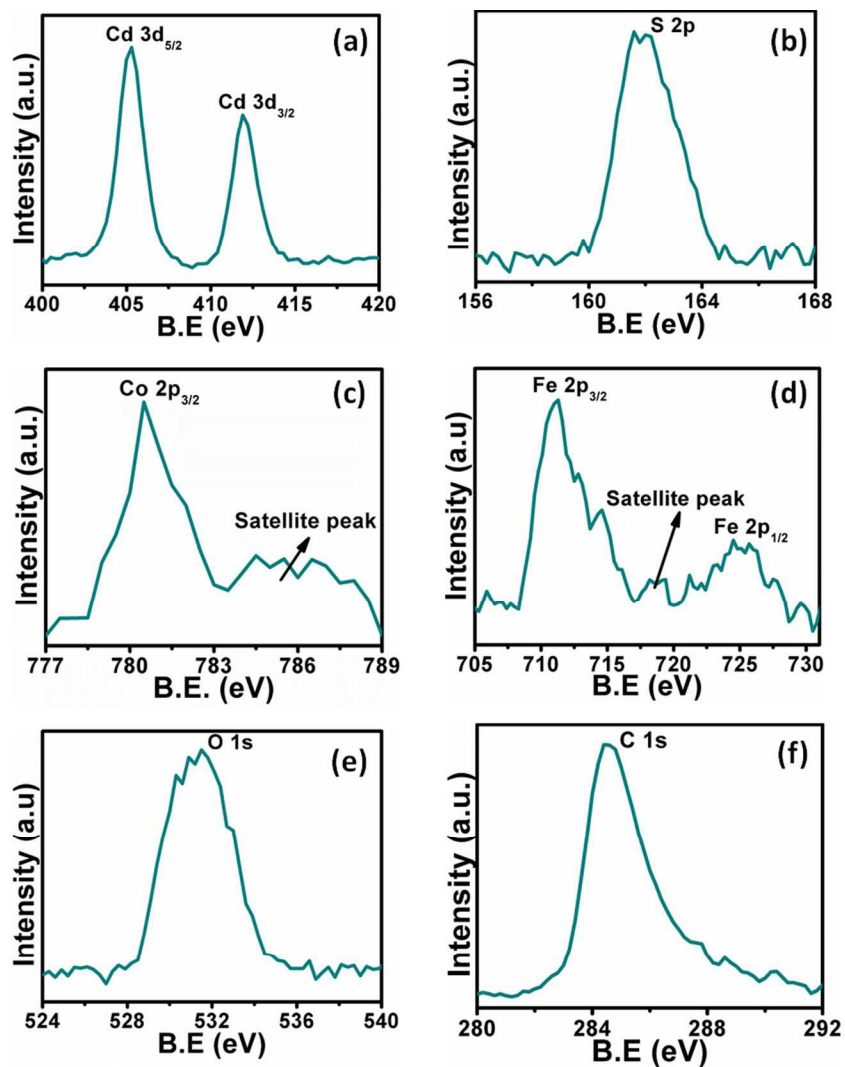


Fig. 3. XPS scans of (a) Cd 3d, (b) S 2p, (c) Co 2p, (d) Fe 2p, (e) O 1s and (f) C 1s in the CdS/CFO/RGO nanostructure.

The XPS spectrum of Co 2p (Fig. 3c) exhibit main peak located at 780.5 eV ($2p_{3/2}$) along with the characteristic satellite peak at 786.1 eV. The presence of broad satellite peak confirms the +2

oxidation state of Co elements. Similarly, in the XPS spectrum of Fe 2p (Fig. 3d) peaks centered at 711.1 eV ($2p_{3/2}$) and 725.1 eV ($2p_{1/2}$) along with the characteristic satellite peak between the two peaks confirm the +3 oxidation state of Fe elements. The XPS spectrum of O 1s (Fig. 3e) exhibit a broad peak located at binding energy ~ 531.1 eV corresponding to lattice oxygen of the CoFe_2O_4 matrix. The XPS spectrum of C 1s (Fig. 3f) show no doublet in the carbon peak centered at 284.5 eV which confirm the presence of reduced form of the graphene oxide in the CdS/CFO/RGO nanostructure.

To examine the morphology of the samples, transmission electron microscopy (TEM) and high resolution transmission electron microscopy (HRTEM) studies have been carried out on GO, CdS, CdS/CFO and CdS/CFO/RGO nanostructures.

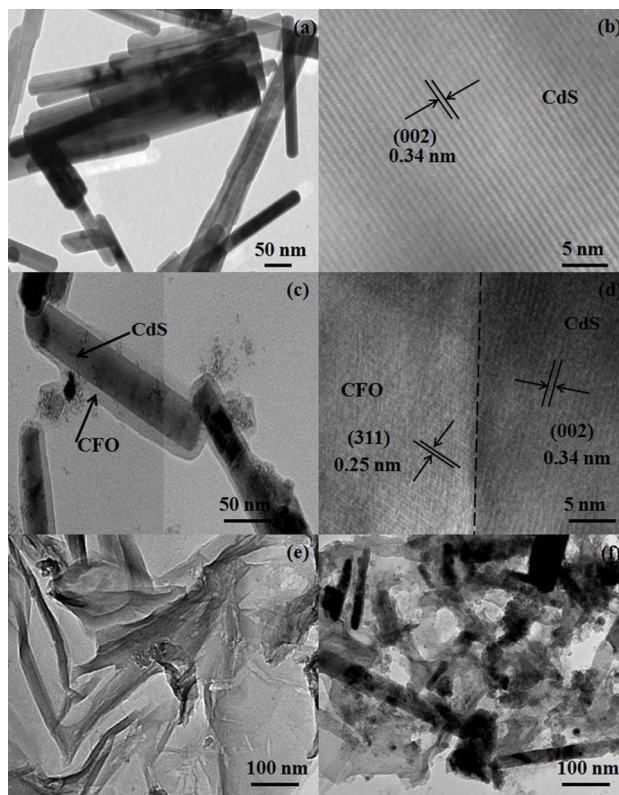


Fig. 4. (a) TEM image of CdS nanorods (b) high resolution TEM image of CdS nanorods (c) TEM image of CdS/CFO core/shell nanorods (d) high resolution TEM image of CdS/CFO nanorods (e) TEM image of GO (f) TEM image of CdS/CFO/RGO nanostructure.

Fig. 4a. shows a TEM image of CdS which shows a rod like structure with the length of the rods as ~200 nm and a diameter of ~35 nm. Lattice fringes determined from the HRTEM image of CdS (Fig. 4b.) shows interplanar spacing of 0.34 nm corresponding to (002) plane of the hexagonal CdS. The formation of the CFO shell of thickness~10 nm around CdS nanorods can be clearly seen in the TEM image of CdS/CFO nanostructure (Fig. 4c.). The HRTEM image of CdS/CFO core/shell nanostructure (Fig. 4d.) shows two distinct sets of lattice fringes of spacing 0.34 nm and 0.25nm corresponds to (002) plane of CdS and (311) plane of CFO, respectively. A uniform interface between the CdS and CFO can be clearly seen in the HRTEM image. Fig. 4e. shows a TEM image of GO which reveals that few layers stacked GO sheets exhibit silk wave like structure. TEM image of the CdS/CFO/RGO nanostructure (Fig. 4f.) shows that the CdS/CFO core/shell nanorods are densely wrapped by RGO sheets.

3.2. Optical bandgap

Fig. 5. shows the Tauc plots for the CFO, CdS, CdS/CFO and CdS/CFO/RGO nanostructures calculated using the relation, $(\alpha h\nu)^2 = A(h\nu - E_g)^{2.9}$

where, E_g is the optical bandgap corresponding to direct allowed transitions, α is the absorption coefficient, $h\nu$ is the absorbed photon energy and A is a constant related to density of electronic states below and above the band gap.

The bandgap values for CFO, CdS, CdS/CFO and CdS/CFO/RGO nanostructures are estimated as 1.86, 2.40, 2.38 and 2.32 eV respectively. The band gap values of CdS/CFO and CdS/CFO/RGO nanostructures are almost similar to that of bare CdS which shows that the coupling of CFO and RGO with CdS exerts no significant change in the bandgap values.

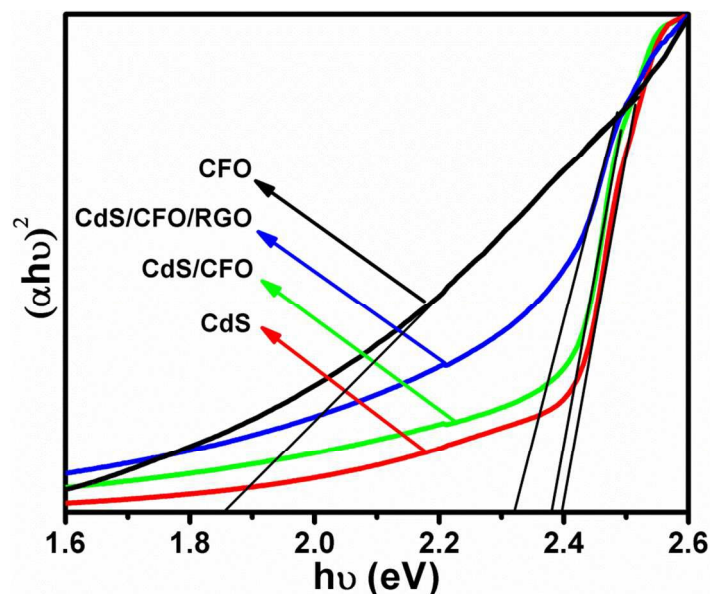


Fig. 5. Tauc Plots for the CFO, CdS, CdS/CFO and CdS/CFO/RGO nanostructures.

3.2.1. Magnetic measurements

Fig. 6. shows M-H loops of CdS/CFO and CdS/CFO/RGO nanostructures at room temperature. For the magnetic measurements we have taken 1 mg of the nanostructure samples. The saturation magnetization and coercivity of CdS/CFO and CdS/CFO/RGO nanostructures are found as 35 emu/g, 600 Oe and 26 emu/g, 680 Oe respectively. The origin of magnetic properties in these composite nanostructures is due to the presence of CFO component.³⁰ As the weight of the two samples taken for the magnetic measurements are same, thus the obtained smaller value of saturation magnetization in CdS/CFO/RGO nanocomposite as compared to CdS/CFO core/shell nanostructure is due to the presence of smaller amount of CFO in CdS/CFO/RGO ternary nanocomposite.

Due to the magnetic nature of CdS/CFO and CdS/CFO/RGO nanostructures, these nanostructures are easily separable from the aqueous solution by applying an external magnetic field. Inset of Fig. 6 shows the magnetic separation of the CdS/CFO/RGO nanostructure from the aqueous solution after the photocatalytic reaction.

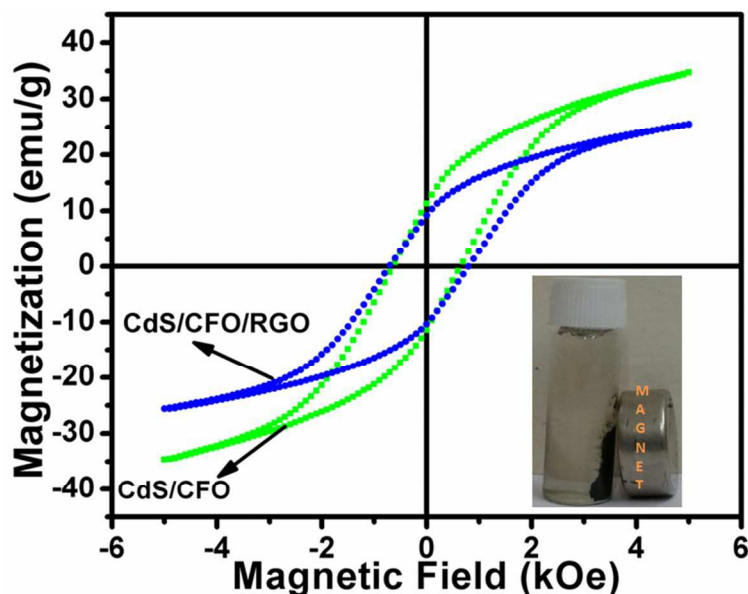


Fig. 6. M-H loops of the CdS/CFO and CdS/CFO/RGO nanostructures at room temperatures. Inset shows the photograph of the separation of the CdS/CFO/RGO nanostructure from the aqueous solution using an external magnetic field.

3.4. Photocatalysis experiment

The photocatalytic performances of the samples were evaluated under visible light irradiation. Fig. 7a. shows the optical absorption spectra of MB dye solution after different durations of exposure to visible light in the presence of CdS/CFO/RGO nanostructures. The decrease in the intensity of the absorption peak of MB in the solution with the increase in the exposure time indicates the decomposition of MB in the aqueous solution. Inset of Fig. 7a. shows a photograph of MB solution when it was exposed to visible light irradiation for different durations of time. The blue color of the solution became almost transparent after 120 minutes of the exposure time, which shows that the MB has fully decomposed. The absorption spectra of MB when it underwent photocatalytic reactions with the CFO, CdS and CdS/CFO nanostructures were also recorded to compare the photocatalytic efficiencies of the nanostructured samples. Fig. 7b. shows the rate of degradation of MB in the presence of CFO, CdS, CdS/CFO and CdS/CFO/RGO nanostructures. The results reveal that the photocatalytic efficiency is much

higher in CdS/CFO/RGO nanostructures as compared to CdS/CFO, CdS and CFO nanostructures. The rate constants for the decomposition of MB are calculated using the relation;³¹

$$\ln \frac{C_0}{C} = kt$$

where C_0 is the initial concentration of MB before illumination, C is the concentration of the MB after different exposures of light irradiation and k is the reaction rate constant.

Fig. 7c. shows the values of the rate constants (k) for the photodecomposition of MB using CFO, CdS, CdS/CFO and CdS/CFO/RGO nanostructures. The CdS/CFO/RGO nanostructure exhibits the highest rate constant value of 0.020 min^{-1} as compared to rate constants for CFO (0.003 min^{-1}), CdS (0.007 min^{-1}) and CdS/CFO (0.011 min^{-1}) nanostructures. The increase in the photocatalytic activity of the CdS/CFO/RGO nanostructure can be attributed to the synergetic effect of CdS/CFO heterostructure and its coupling with RGO which facilitates efficient separation of the photogenerated charge carriers.

Fig. 7d. shows reusability tests of CdS/CFO and CdS/CFO/RGO nanostructures for the photocatalytic reaction with MB. The good photostability of the nanostructures even after five repeated operations of the photocatalytic reaction is evident from the results. The reusability of the nanostructures is possible due to the magnetic nature of the composite nanostructures which result in easy separation of these nanostructures from the water treating system by applying an external magnetic field. The repeated utilization of the photocatalyst material is a great advantage as it makes the process more economical.

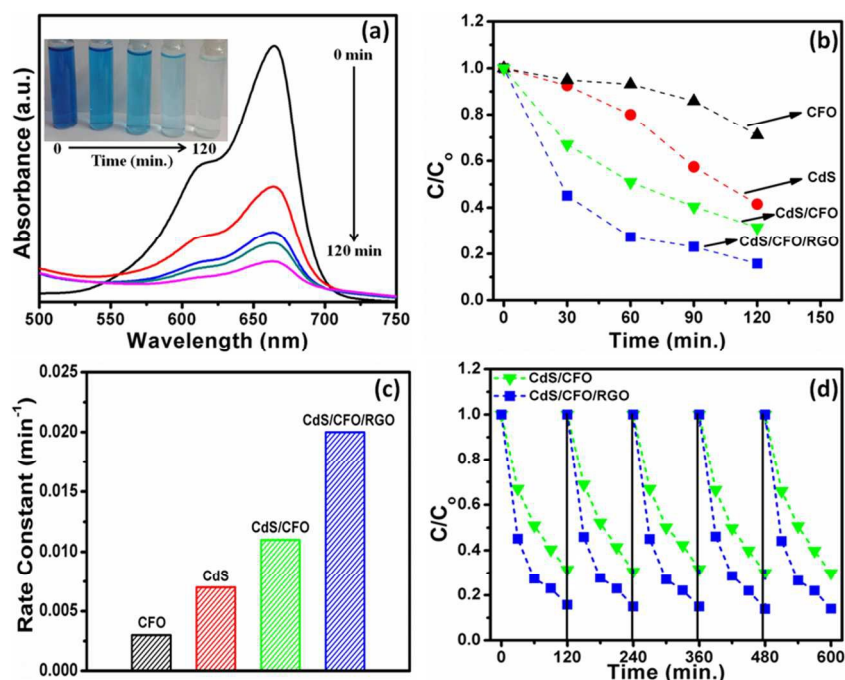


Fig. 7. (a) UV-visible absorption spectra of MB in aqueous solution in the presence of CdS/CFO/RGO nanostructures as a function of irradiation time (inset shows photographs of the MB solution after different duration of visible light exposure), (b) Comparison of the photocatalytic efficiency of CFO, CdS, CdS/CFO and CdS/CFO/RGO nanostructures for the photodegradation of MB, (c) Comparison of the values of the rate constants for the degradation of MB, (d) Degradation of MB dye using CdS/CFO and CdS/CFO/RGO nanostructures for five recycles.

3.5 Photoelectrochemical measurements

For evaluating the separation capability of the photogenerated electron-hole pairs in the CdS, CdS/CFO and CdS/CFO/RGO nanostructures, we performed photoelectrochemical measurements on these samples. For these measurements, thin films of nanostructure materials were prepared by coating nanostructure semiconductors on FTO substrates which act as working electrodes. Fig. 8a. shows the linear sweep voltammograms (LSVs) of the samples under dark and visible light irradiation ($\lambda > 420$ nm) of intensity 100 mW/cm^2 . The CdS/CFO/RGO nanostructure is found to exhibit maximum photocurrent density of 23 mA/cm^2 at 1 V vs Ag/AgCl which is about ~ 4.5 times higher than bare CdS nanorods and ~ 2.5 times higher than

CdS/CFO nanohybrid. This clearly indicates that CdS/CFO/RGO nanostructure has higher efficiency for the separation of the photogenerated electron-hole pairs as compared to CdS and CdS/CFO nanostructures. In addition, electrochemical impedance spectroscopy (EIS) has also been carried out to interpret the enhancement in the photocurrent density in CdS/CFO and CdS/CFO/RGO nanostructures as compared to CdS nanostructures. Fig. 8b. show the EIS Nyquist plots for CdS, CdS/CFO and CdS/CFO/RGO nanostructures. The charge transfer resistance (R_{ct}) and the corresponding capacitance (C_{dl}) at the electrode-electrolyte interface is estimated by fitting the semi arcs with ZView software using an equivalent circuit model as shown in the inset of Fig. 8b. The diameter of the semi arc represents the charge transfer resistance at the electrode surface.³²⁻³⁴ For the CdS, CdS/CFO and CdS/CFO/RGO nanostructures the values for R_{ct} and C_{dl} are found to be 10.7 k Ω , 2 k Ω , 0.7 k Ω and 26 μ F, 88 μ F, 523 μ F respectively. It is evident the R_{ct} value for the CdS/CFO/RGO nanostructure is smallest as compared to CdS/CFO and CdS nanostructures which again indicates high separation capability of the photogenerated charge carriers in this ternary nanocomposite.

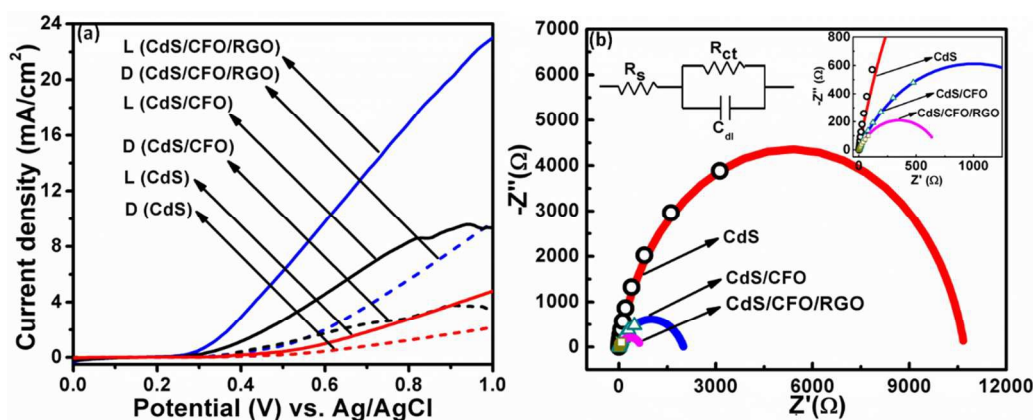


Fig. 8. (a) Current-potential curves of the CdS, CdS/CFO and CdS/CFO/RGO nanostructures under dark (D; dotted line plots) and under visible light irradiation (L; solid line plots) using 0.5 M Na₂SO₄ as an electrolyte, (b) Electrochemical impedance spectroscopy Nyquist plots of CdS, CdS/CFO and CdS/CFO/RGO nanostructures. Inset of the figure shows the equivalent circuit model and magnified view of the impedance spectra.

3.6 Photoluminescence measurements

To further probe the recombination process of the photogenerated electron-hole pairs in the semiconductor nanostructures, we performed Photoluminescence (PL) spectroscopy for all the samples. Fig. 9. shows the PL spectra of CdS, CdS/CFO and CdS/CFO/RGO nanostructures at room temperature.

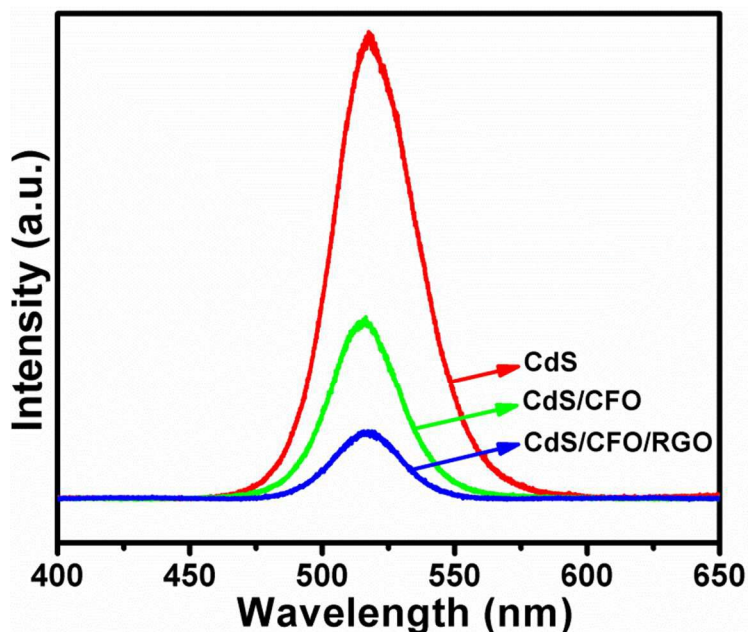


Fig. 9. Photoluminescence spectra of CdS, CdS/CFO and CdS/CFO/RGO nanostructures at room temperature.

The PL spectrum for the CdS exhibit an emission peak at ~506 nm which can be ascribed to the near band edge emission arising due to the recombination of electron hole-pairs. The PL spectra for CdS/CFO and CdS/CFO/RGO nanostructures consist of similar emission peak corresponding to CdS but the intensity of the peak is reduced as compared to the peak intensity of bare CdS. The decrease in the intensity of the peak corresponding to CdS in the CdS/CFO and CdS/CFO/RGO nanostructures can be due to the formation of interfaces between CdS and CFO and between CdS/CFO and RGO respectively, which result in the efficient separation of the

photogenerated charge carriers leading to suppression of the recombination of photogenerated electron-hole pairs.³⁵⁻³⁷

3.7. Photocatalysis reaction mechanism.

To investigate the reaction mechanism for the enhanced separation of the photogenerated charge carriers in CdS/CFO and CdS/CFO/RGO nanostructures, the conduction band (CB) and valence band (VB) positions of the CdS and CFO semiconductor nanostructures are calculated by using the following empirical equations,³⁸

$$E_{CB} = X + E_o - 0.5E_g$$

and

$$E_{VB} = E_{CB} + E_g$$

where E_{CB} is the conduction band potential, E_{VB} is the valence band potential, E_g is the semiconductor band gap energy, E_o is the energy of the free electrons on the hydrogen scale (~ -4.5 eV), and X is the electronegativity of semiconductor which can be calculated by using the geometric mean of the absolute electronegativity of the constituent atoms. The calculated CB and VB potentials of CdS and CFO are summarized in Table 1.

Table 1. Calculated values of the conduction band and valence band positions of the CdS, CFO and CdS/CFO core/shell nanoheterostructure.

Sample	Bandgap (eV)	Conduction band (eV) w.r.t NHE	Valence band (eV) w.r.t NHE
CdS	2.4	-0.60	1.80
CFO	1.86	0.38	2.24

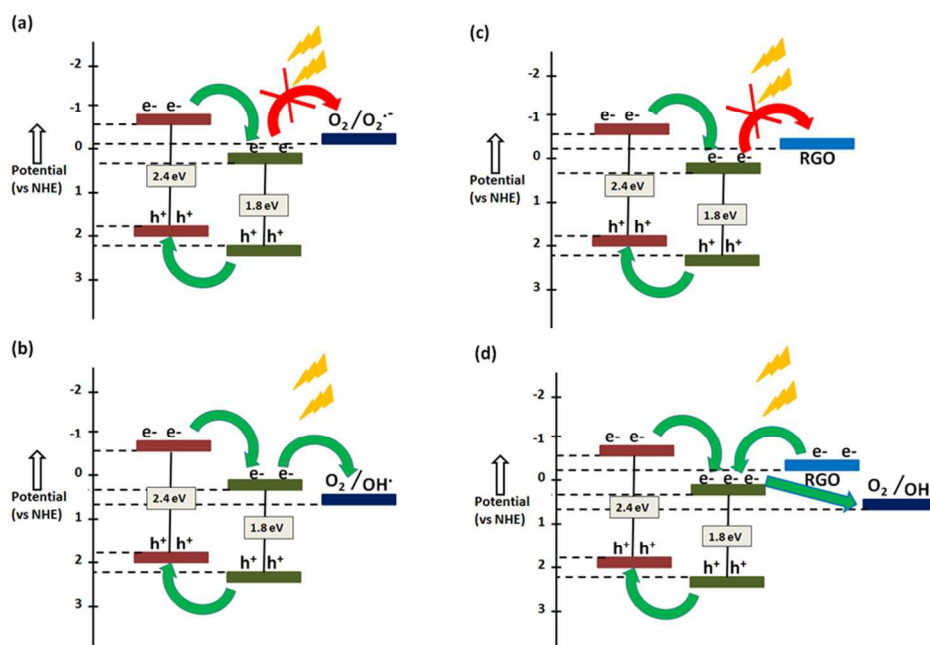
The CB and VB positions of CdS are at higher potential as compared to CFO thus forming a staggered type-II heterojunction between CdS and CFO. Under visible light irradiation, the

electrons are transferred from the conduction band of CdS to the conduction band of the CFO and the holes are transferred from the valence band of the CFO to the valence band of CdS and thereby retarding the recombination of the photogenerated charge carriers and thus enhancing the photocatalytic degradation of organic dye molecules. It is well known that the hydroxyl radicals are the main reactive species for the degradation of organic dyes. The generation of hydroxyl radicals ($\text{OH}\cdot$) after the photoexcitation of semiconductors can be due to the following pathways: (i) the photogenerated holes in the valence band (h_{VB}^+) of the semiconductor react with the water molecules (H_2O) to generate $\text{OH}\cdot$ radicals, (ii) the electrons in the conduction band (e_{CB}^-) of the semiconductor react with the surface oxygen (O_2) to generate superoxide anion radicals (O_2^-) and these O_2^- radicals undergo subsequent reactions with the water molecules to generate finally the $\text{OH}\cdot$ radicals.

In the present case, due to the conduction band position of CFO (0.38 eV vs. NHE), the generation of O_2^- radicals is not feasible because the electrons transferred to the CB of CFO do not have sufficient potential to reduce O_2 [$E^\circ (\text{O}_2/\text{O}_2^-) = -0.046$ eV vs NHE)] to generate O_2^- radicals³⁸ and thus cannot participate in the photocatalytic reaction (Scheme 2a). The other possible pathway for the electrons to participate in the photodegradation reaction is the multielectron reduction [$E^\circ (\text{O}_2/\text{H}_2\text{O}_2) = 0.69$ eV vs NHE)] of oxygen to generate hydroxyl radicals (Scheme 2b).³⁹ Also, due to small thickness of the CFO, the photogenerated holes from CdS are able to tunnel out to generate the hydroxyl radicals;³⁹



Further, the higher photocatalytic activity is achieved after the coupling of RGO with CdS/CFO nanostructure, which is attributed to the higher separation capability of the photogenerated charge carriers. However, the conduction band (C.B) positions and work function of CdS (-0.6 eV vs NHE), CFO (0.38 eV vs NHE) and RGO (-0.08 eV vs NHE) respectively, are such that the photogenerated electrons transferred from the CB of CdS to the CB of CFO cannot be further transferred to RGO due to its lower work function (Scheme 2c). Under these circumstances, the CdS/CFO/RGO nanocomposite should not exhibit enhanced photocatalytic activity as compared to CdS or CdS/CFO nanostructures. Thus, for the observed enhanced photocatalytic activity a possible reaction mechanism for the ternary CdS/CFO/RGO nanostructure is proposed (Scheme 2d) where a role of RGO as a visible light responsive photosensitizer has been shown which is absolutely different from the conventional role of the RGO, as an electron acceptor and transporter, reported in most of the RGO-semiconductor nanocomposites.



Scheme 2. Schematic band diagrams of the reaction mechanism of charge transfer in CdS/CFO (a and b) and CdS/CFO/RGO (c and d) nanostructures.

According to this, when the visible light is irradiated on the CdS/CFO/RGO nanostructure, the electrons are transferred from the CB of CdS to the CB of CFO and also the electrons generated in RGO under visible light irradiation are transferred to the CB of CFO. This would result in enhanced generation of $\text{OH}\cdot$ radicals through reaction 1 & 2 and thus result in higher efficiency for the photocatalytic degradation of MB dye.

To determine the dominant active species responsible for the degradation of MB, a series of control experiments using different radical scavengers have been conducted. Fig. 10 shows the photodegradation efficiency of CdS/CFO/RGO nanostructure in the presence of benzoquinone (BQ), tert-butyl alcohol (TBA) and ammonium oxalate (AO) as scavengers for superoxide anion radicals, hydroxyl radicals and holes respectively. The photodegradation activity was negligibly altered in the presence of BQ which shows that superoxide anion radicals are not the dominant active species for the degradation of MB. However, when TBA was used as a scavenger for hydroxyl radicals in the reaction system the degradation of MB was greatly reduced. Thus, the results indicate that the dominant active species for the enhanced photocatalytic activity of the CdS/CFO/RGO nanostructure are due to generation of more hydroxyl radicals. Ammonium (AO) oxalate was used as a hole scavenger to estimate the role of holes in the photocatalytic degradation of MB. In the presence of ammonium oxalate, the photocatalytic activity was reduced which shows that holes also participate to generate the hydroxyl radicals for the degradation of MB dye. As described in reaction 2 & 3, the hydroxyl radicals can be generated by photoelectrons or by photoholes. In the hole scavenger experiment, we noticed a decrease in the photocatalytic degradation efficiency by $\sim 28\%$ which indicates that in the present case

photogenerated electrons play a major role in the generation of hydroxyl radicals which causes degradation of MB.

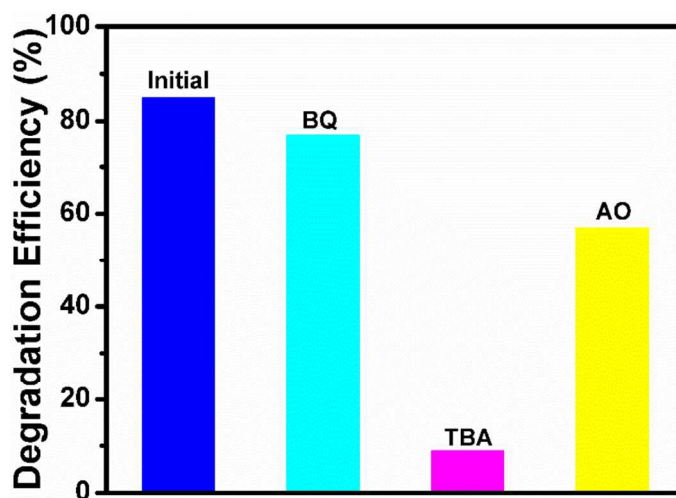


Fig. 10. Controlled experiments for the photodegradation of MB using CdS/CFO/RGO nanostructure in the presence of benzoquinone (BQ, scavenger for superoxide anion radicals), tert-butyl alcohol (TBA, scavenger for hydroxyl radicals) and ammonium oxalate (AO, scavenger for holes) under visible light irradiation.

3.8. Stability test

Along with high photocatalytic activity, the stability of a photocatalyst material is also of great importance for its practical applications. To check the stability of the photocatalyst materials after performing the photocatalytic activities for five cycles, we again performed XRD for the structural analysis of the photocatalyst materials. Fig. 11 shows the XRD patterns of CdS, CdS/CFO and CdS/CFO/RGO nanostructures after performing 5 cycles of the photocatalytic reaction. It is found that CdS is decomposed due to photocorrosion in the aqueous solution, but CdS/CFO core/shell nanostructure as well as CdS/CFO/RGO nanostructure does not photocorrode due to the presence of stable CFO cap layer over the CdS nanorods.

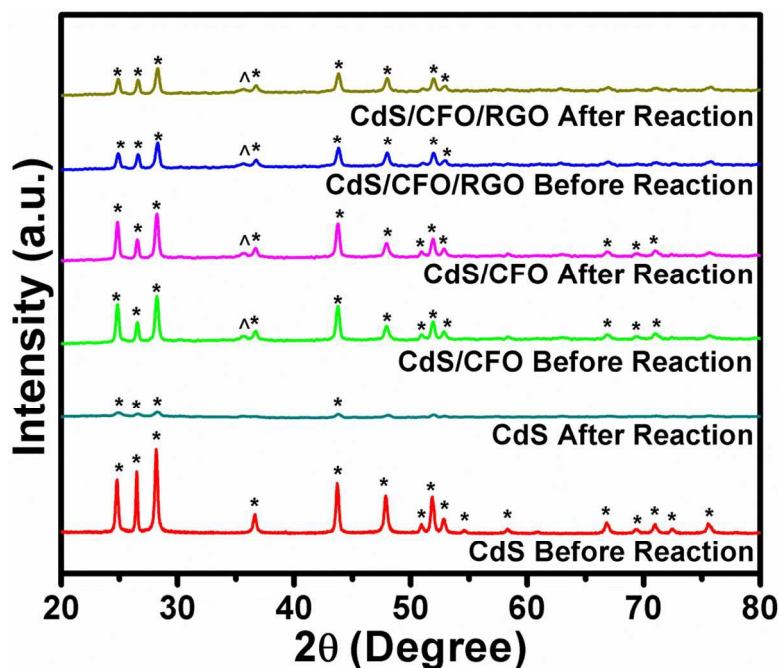


Fig. 11. XRD patterns of the CdS, CdS/CFO and CdS/CFO/RGO nanostructures before photocatalytic reaction and after photocatalytic reaction. The peaks marked with (*) corresponds to CdS and peaks marked with (^) corresponds to CFO.

4. Conclusions

In summary, we have synthesized a CdS/CFO/RGO ternary nanohybrid where a synergetic effect of CdS/CFO semiconductor nanoheterostructure and a role of RGO as a visible light responsive photosensitizer have been demonstrated for the enhanced photocatalytic degradation of methylene blue. The magnetic nature of CFO in the ternary nanohybrid results in its easy separation from the reaction system after the photocatalytic activity. Also, the coating of CFO around CdS in the CdS/CFO/RGO nanocomposite protects CdS from photocorrosion due to excellent chemical stability of CFO which results in efficient reusability of this trio coupled nanocomposite for repeated operation of the photocatalytic reactions.

Acknowledgements

The financial support from DeitY (Govt. of India) (RP02395) and DST-UKIERI (RP02893) projects are gratefully acknowledged.

References:

- 1 G. Zhang, M. Zhang, X. Ye, X. Qiu, S. Lin and X. Wang, *Adv. Mater.*, 2014, **26**, 805.
- 2 F. Iskandar, A. B. D. Nandiyanto, K. M. Yun, C. J. Hogan, Jr., K. Okuyama and P. Biswas, *Adv. Mater.*, 2007, **19**, 1408.
- 3 S. Weng, Z. Pei, Z. Zheng, J. Hu and P. Liu, *ACS Appl. Mater. Interfaces*, 2013, **5**, 12380.
- 4 J. B. Varley, A. Janotti and C. G. V. Walle, *Adv. Mater.*, 2011, **23**, 2343.
- 5 V. Etacheri, R. Roshan and V. Kumar, *ACS Appl. Mater. Interfaces*, 2012, **4**, 2717.
- 6 Z. Xu, M. Quintanilla, F. Vetrone, A. O. Govorov, M. Chaker and D. Ma, *Adv. Funct. Mater.*, 2015, DOI: 10.1002/adfm.201500810.
- 7 H. N. Tien, V. H. Luan, L. T. Hoa, N. T. Khoa, S. H. Hahn, J. S. Chung, E. W. Shin and S. H. Hur, *Chem. Eng. J.*, 2013, **229**, 126.
- 8 H. Li, Y. Zhou, W. Tu, J. Ye and Z. Zou, *Adv. Funct. Mater.*, 2015, **25**, 998.
- 9 R. Marschall, *Adv. Funct. Mater.*, 2014, **24**, 2421.
- 10 Y. Wang, Q. Wang, X. Zhan, F. Wang, M. Safdar and J. He, *Nanoscale*, 2013, **5**, 8326.
- 11 M. Niu, F. Huang, L. Cui, P. Huang, Y. Yu and Y. Wang, *ACS Nano*, 2010, **4**, 681.
- 12 S. Kumar, A. Baruah, S. Tonda, B. Kumar, V. Shanker and B. Sreedhar, *Nanoscale*, 2014, **6**, 4830.
- 13 L. Zhang, Y. Li, Q. Zhang and H. Wang, *Cryst. Eng. Comm.*, 2013, **15**, 5986.
- 14 Y. Tian, B. Chang, J. Lu, J. Fu, F. Xi and X. Dong, *ACS Appl. Mater. Interfaces*, 2013, **5**, 7079.
- 15 G. Xie, K. Zhang, B. Guo, Q. Liu, L. Fang and J. R. Gong, *Adv. Mater.*, 2013, **25**, 3820.
- 16 W. Tu, Y. Zhou and Z. Zou, *Adv. Funct. Mater.*, 2013, **23**, 4996.
- 17 L. Yuan, M. Q. Yang and Y. J. Xu, *Nanoscale*, 2014, **6**, 6335.

- 18 Y. Zhang, N. Zhang, Z. R. Tang and Y. J. Xu, *ACS Nano*, 2012, **6**, 9777.
- 19 J. C. Johannsen, S. Ulstrup, A. Crepaldi, F. Cilento, M. Zacchigna, J. A. Miwa, C. Cacho, R. T. Chapman, E. Springate, F. Fromm, C. Raidel, T. Seyller, P. D. C. King, F. Parmigiani, M. Grioni and P. Hofmann, *Nano Lett.*, 2015, **15**, 326.
- 20 A. Du, Y. H. Ng, N. J. Bell, Z. Zhu, R. Amal, S. C. Smith, *J. Phys. Chem. Lett.*, 2011, **2**, 894.
- 21 J. Sha, N. Zhao, E. Liu, C. Shi, C. He and J. Li., *Carbon*, 2014, **68**, 352.
- 22 Md. S. A. S. Shah, K. Zhang, A. R. Park, K. S. Kim, N. G. Park, J. H. Park and P. J. Yoo, *Nanoscale*, 2013, **5**, 5093.
- 23 J. Wang, P. Wang, Y. Cao, J. Chen, W. Li, Y. Shao, Y. Zheng and D. Li. *Appl. Catal. B*, 2013, **136**, 94.
- 24 X. X. Wei, C. M. Chen, S. Q. Guo, F. Guo, X. M. Li, X. X. Wang, H. T. Cui, L. F. Zhao and W. Li, *J. Mater. Chem. A*, 2014, **2**, 4667.
- 25 Q. Xiang, J. Yu and M. Jaroniec, *J. Am. Chem. Soc.*, 2012, **134**, 6575.
- 26 P. Kumar, N. Saxena, R. Chandra, V. Gupta, A. Agarwal and D. Kanjilal, *Nanoscale Res. Lett.*, 2012, **7**, 584.
- 27 Z. Ji, X. Shen, M. Li, H. Zhou, G. Zhu and K. Chen, *Nanotechnology*, 2013, **24**, 115603.
- 28 Q. P. Luo, X. Y. Yu, B. X. Lei, H. Y. Chen, D. B. Kuang and C. Y. Su, *J. Phys. Chem. C*, 2012, **116**, 8111.
- 29 J. A. Glasscock, P. R. F. Barnes, I. C. Plumb, A. Bendavid and P. J. Martin, *Thin Solid Films*, 2008, **516**, 1716.
- 30 S. Singh, S. Munjal, N. Khare, *J. Magn. Magn. Mater.*, 2015, **386**, 69.

- 31 S. Zhang, F. Ren, W. Wu, J. Zhou, L. Sun, X. Xiao and C. Jiang, *J. Colloids Interf Sci.*, 2014, **427**, 29.
- 32 H. Zhang, X. Lv, Y. Li, Y. Wang and J. Li, *ACS Nano*, 2010, **4**, 380.
- 33 T. W Lin, C. J. Liu and J. Y. Lin, *Appl. Catal., B: Environ.* 2013, **134**, 75.
- 34 J. Kubisztal, A. Budniok and A. Lasia, *Int. J. Hydrogen Energy*, 2007, **32**, 1211.
- 35 Y. B. Shahar, F. Scotognella, N. Waiskopf, I. Kriegel, S. D. Conte, G. Cerullo and U. Banin, *Small*, 2015, **11**, 462.
- 36 W. T. Chen, T. T. Yang and Y. J. Hsu, *Chem. Mater.*, 2008, **20**, 7204.
- 37 Z. Wang, C. Yang, T. Lin, H. Yin, P. Chen, D. Wan, F. Xu, F. Huang, J. Lin, X. Xie and M. Jiang, *Adv. Funct. Mater.*, 2013, **23**, 5444.
- 38 L. Ye, Y. Su, X. Jin, H. Xie and C. Zhang, *Environ. Sci.: Nano*, 2014, **1**, 90.
- 39 J. Kim, C. W. Lee and W. Choi, *Environ. Sci. Technol.*, 2010, **44**, 6849.

Figure Caption:

- Scheme 1a.** Schematic diagram showing different steps in the synthesis of CdS/CFO core/shell nanostructure.
- Scheme 1b.** Schematic diagram for the synthesis of CdS/CFO/RGO nanostructure.
- Scheme 2.** Schematic band diagrams of the reaction mechanism of charge transfer in CdS/CFO (a and b) and CdS/CFO/RGO (c and d) nanostructures.
- Fig. 1.** (a) XRD patterns of the CFO, CdS, CdS/CFO and CdS/CFO/RGO nanostructures. In the core/shell nanostructures, peaks marked with (*) corresponds to CdS and peaks marked with (^) correspond to CFO. (b) Shift in the peak position of the (110) peak of CdS in the CdS/CFO and CdS/CFO/RGO nanostructures.
- Fig. 2.** Raman spectra of CdS, CdS/CFO, CdS/CFO/RGO and GO nanostructures at room temperature.
- Fig. 3.** XPS scans of (a) Cd 3d, (b) S 2p, (c) Co 2p, (d) Fe 2p, (e) O 1s and (f) C 1s in the CdS/CFO/RGO nanostructure.
- Fig. 4.** (a) TEM image of CdS nanorods (b) high resolution TEM image of CdS nanorods (c) TEM image of CdS/CFO core/shell nanorods (d) high resolution TEM image of CdS/CFO nanorods (e) TEM image of GO (f) TEM image of CdS/CFO/RGO nanostructure.
- Fig. 5.** Tauc Plots for the CFO, CdS, CdS/CFO and CdS/CFO/RGO nanostructures.
- Fig. 6.** M-H loops of the CdS/CFO and CdS/CFO/RGO nanostructures at room temperatures. Inset shows the photograph of the separation of the CdS/CFO/RGO nanostructure from the aqueous solution using an external magnetic field.

- Fig. 7.** (a) UV-visible absorption spectra of MB in aqueous solution in the presence of CdS/CFO/RGO nanostructures as a function of irradiation time (inset shows photographs of the MB solution after different duration of visible light exposure), (b) Comparison of the photocatalytic efficiency of CFO, CdS, CdS/CFO and CdS/CFO/RGO nanostructures for the photodegradation of MB, (c) Comparison of the values of the rate constants for the degradation of MB, (d) Degradation of MB dye using CdS/CFO and CdS/CFO/RGO nanostructures for five recycles.
- Fig. 8.** (a) Current-potential curves of the CdS, CdS/CFO and CdS/CFO/RGO nanostructures under dark (D; dotted line plots) and under visible light irradiation (L; solid line plots) using 0.5 M Na₂SO₄ as an electrolyte, (b) Electrochemical impedance spectroscopy Nyquist plots of CdS, CdS/CFO and CdS/CFO/RGO nanostructures. Inset of the figure shows the equivalent circuit model and magnified view of the impedance spectra.
- Fig. 9.** Photoluminescence spectra of CdS, CdS/CFO and CdS/CFO/RGO nanostructures at room temperature.
- Fig. 10.** Controlled experiments for the photodegradation of MB using CdS/CFO/RGO nanostructure in the presence of benzoquinone (BQ, scavenger for superoxide anion radicals), tert-butyl alcohol (TBA, scavenger for hydroxyl radicals) and ammonium oxalate (AO, scavenger for holes) under visible light irradiation.
- Fig. 11.** XRD patterns of the CdS, CdS/CFO and CdS/CFO/RGO nanostructures before photocatalytic reaction and after photocatalytic reaction. The peaks marked with (*) corresponds to CdS and peaks marked with (^) corresponds to CFO.

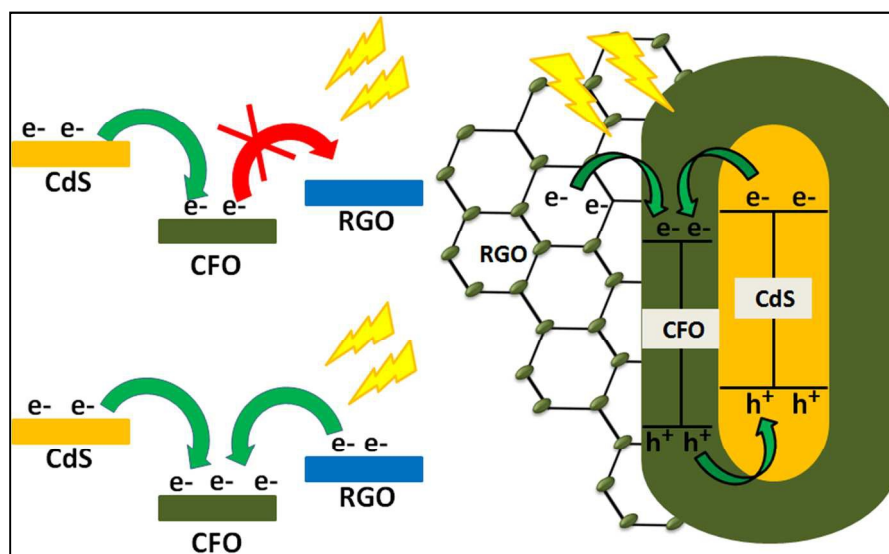
Table Caption:

Table 1. Calculated values of the conduction band and valence band positions of the CdS, CFO and CdS/CFO core/shell nanoheterostructure.

Graphical Abstract

Reduced Graphene Oxide Coupled CdS/CoFe₂O₄ Ternary Nanohybrid for Enhanced Photocatalytic Activity and Stability: A Potential Role of Reduced Graphene Oxide as a Visible Light Responsive Photosensitizer

Simrjit Singh and Neeraj Khare



CdS/CFO core/shell nanoheterostructure coupled with reduced graphene oxide (RGO) exhibits much enhanced photocatalytic activity as compared to CdS/CFO and CdS nanostructures. The coupling of RGO with CdS/CFO nanostructure serves as a visible light responsive photosensitizer which account for the observed enhancement in the photocatalytic activity of ternary CdS/CFO/RGO nanostructure. The presence of CFO component as a shell around CdS nanorods improves the photostability of the ternary nanocomposite and also helps in its easy separation from the aqueous solution after the photoreaction by applying an external magnetic field.